Acta Materialia 180 (2019) 180–188

Contents lists available at ScienceDirect

Acta Materialia

journal homepage: www.elsevier.com/locate/actamat

Resistance to amorphisation in $Ca_{1-x}La_{2x/3}TiO_3$ perovskites – a bulk ion-irradiation study

Sebastian M. Lawson [a, *], Neil C. Hyatt [a], Karl R. Whittle [a, b], Amy S. Gandy [a]

[a] Immobilisation Science Laboratory, Department of Materials Science and Engineering, University of Sheffield, Sheffield, S1 3JD, United Kingdom
[b] School of Engineering, University of Liverpool, Liverpool, L69 3GH, United Kingdom

ARTICLE INFO

Article history:
Received 30 May 2019
Received in revised form
3 September 2019
Accepted 5 September 2019
Available online 10 September 2019

Keywords:
Perovskite
Nuclear materials
Radiation damage

ABSTRACT

The changes induced from 1 MeV Kr^+ and 5 MeV Au^+ ion irradiation at room temperature have been utilised to determine the impact of cation vacancies on the radiation damage response of bulk $Ca_{1-x}La_{2x/3}TiO_3$ perovskite structured ceramics. Perovskite systems have long been considered as candidate waste forms for the disposition of actinide wastes, and doping with multi-valent elements such as Pu may lead to cation deficiency. Based on GAXRD and TEM analysis, two regions of resistance/susceptibility to amorphisation have been confirmed with reference to $CaTiO_3$. Increased resistance to amorphisation has been observed for $0.1 \leq x \leq 0.4$, with an increased susceptibility to amorphisation for $x \geq 0.5$. It is proposed that these processes are induced by enhanced recovery from radiation damage for $0.1 \leq x \leq 0.4$, and reduced tolerance for disorder/the increasingly covalent nature of the A-O bond for $x \geq 0.5$. Lattice parameter analysis of the $x = 0$ and 0.5 samples showed a saturation in radiation damage induced volume swelling at $4.7 \pm 0.1\%$ and $1.8 \pm 0.1\%$, respectively, while the saturation limit for the *b* parameter was lower than the respective *a* and *c* orthorhombic parameters. In the $x = 0.2$ and 0.4 samples, amorphisation was not observed, however the *b* parameter was found to swell to a lesser extent than the *a* and *c* parameters. Swelling was not observed for the ion irradiated $x \geq 0.6$ samples.

1. Introduction

A-site cation deficiency in perovskites has been studied widely and exploited to produce perovskites suitable across a range of applications. These include anodes for solid oxide fuel cells [1,2], memory storage [3] and dielectric resonators [4], while perovskite was a constituent of the SYNROC study for the disposition of high-level nuclear waste [5–7]. The potential to use perovskites as an actinide baring ceramic phase has been extensively investigated [7–16], and is a potential secondary Pu host phase in ceramics for immobilisation in the UK stockpile [17]. Perovskites take the general chemical formula ABO_3, and it has been proposed that doping the perovskite A-site with multi-valent uranium and plutonium ions leads to A-site cation deficiency through charge compensation [18]. Characterisation of the effects of A-site deficiency is a key factor in understanding the long-term material properties of doped perovskites in a nuclear waste form disposal environment.

Perovskites have previously shown intriguing behaviour under irradiation, including phase transitions prior to amorphisation in $CaTiO_3$ [12,16,19] and $SrTiO_3$ [20]. Recently, studies have focused on understanding radiation damage recovery mechanisms in A-site deficient perovskites. Smith et al. [21] first reported the critical temperature of amorphisation, T_c, in the $Sr_{1-x}La_{2x/3}TiO_3$ system using *in-situ* ion irradiation in a TEM. Above T_c, damage annealing rates exceed induced damage rates, preventing amorphisation in crystalline materials. Within the $0.1 \leq x \leq 0.3$ regime, a reduction in T_c was reported relative to the T_c for $SrTiO_3$, whereas T_c was found to increase with increasing La content from $x \geq 0.45$. The authors proposed a possible mechanism for this phenomena, with increased A-site vacancy defect mobility induced by La doping leading to the reductions in T_c. They further proposed that as reductions in T_c were only observed in the *Pm-3m* cubic structure, the distorted octahedral networks of the *I4/mcm* and *Cmmm* phases produced by stoichiometries of $x \geq 0.45$ hindered defect migration and inhibit damage recovery. More recently, Whittle et al. [22] conducted equivalent *in-situ* experiments in the counterpart $Ca_{1-x}La_{2x/3}TiO_3$ system, again observing a decrease in T_c, relative to $CaTiO_3$, in the range $0.1 \leq x \leq 0.3$. However, in this instance decreases in T_c were observed within the orthorhombic *Pbnm* phase

* Corresponding author.
E-mail address: m.s.lawson@sheffield.ac.uk (S.M. Lawson).

https://doi.org/10.1016/j.actamat.2019.09.006

with highly distorted octahedral tilting present, providing further evidence that A-site vacancies play a key role in the decreased values of T_c. This was further linked to the ability of the samples in the $0.1 \leq x \leq 0.3$ regime to accommodate disorder compared to those for $x \geq 0.5$. In this study we have investigated further the response of $Ca_{1-x}La_{2x/3}TiO_3$ to heavy ion irradiation, used as an analogue for alpha-recoil nuclei, in bulk samples in order for more detailed structural analysis to be carried out.

Structural characterisation of the $Ca_{1-x}La_{2x/3}TiO_3$ system has previously been reported. Phase transitions in the $Ca_{1-x}La_{2x/3}TiO_3$ solid-solution were reported by Vashook et al. [1,2] using synchrotron X-ray diffraction (XRD) and later refined by Zhang et al. [23] using neutron diffraction. Structures are reported as *Pbnm* ($a^-a^-c^+$, using Glazer notation [24]) for $0 \leq x \leq 0.5$; *Ibmm* ($a^-a^-c^0$) for $x = 0.6$; *I4/mcm* ($a^0a^0c^-$) for $0.7 \leq x \leq 0.8$; and *Cmmm* ($a^-b^0c^0$) for $0.8 \leq x \leq 0.96$. These structures are graphically represented in Fig. 1. Furthermore, short-range A-site vacancy and cation ordering is reported in the $x = 0.7$ and 0.8 samples by Zhang et al. [23], with long-range ordering reported in the $x = 0.9$ sample. This was confirmed by Danaie et al. [25], observing long-range cation/vacancy ordering in the $x = 0.9$ sample using high-resolution scanning transmission electron microscopy. Ordering of this nature occurs as alternating layers of cation deficient and cation rich A-site planes, and has been previously observed in the sister $Sr_{1-x}La_{2x/3}TiO_3$ system for $x \geq 0.7$ [26] and the A-site deficient $La_{1/3}NbO_3$ and $La_{1/3}TaO_3$ compounds [27].

The work conducted by Smith et al. [21] and Whittle et al. [22] demonstrates that damage recovery in these systems is not simply due to crystal structure, and that vacancy content may play an integral role. These studies were carried out at variable temperatures (<900 K) on thin, typically ~100 nm, electron transparent samples *in-situ* in a TEM. Thus whilst both dynamical and thermal annealing were investigated, the damage recovery process may not be fully representative of the bulk due to the proportionally high surface area acting as a sink for defects. In this study we have investigated the impact of vacancies on damage recovery in bulk $Ca_{1-x}La_{2x/3}TiO_3$ samples, and observed irradiation induced volume swelling prior to amorphisation following room temperature Kr^+ and Au^+ ion irradiations. Cross-sectional transmission electron microscopy (XTEM), including electron diffraction pattern analysis, and glancing-angle X-ray diffraction (GAXRD) have been used to elucidate the behaviour of A-site deficient perovskites under heavy ion irradiation.

2. Experimental methods

2.1. Sample synthesis

Pellets of the $Ca_{1-x}La_{2x/3}TiO_3$ system ($x = 0, 0.1 \ldots 0.9$) were prepared by solid-state synthesis. Stoichiometric amounts of La_2O_3 (Alfa Aesar 99.99%), dried at 1073 K for 24 h, TiO_2 (Sigma-Aldrich 99.9%) and $CaCO_3$ (Alfa Aesar 99.9%), both dried at 453 K for 24 h, were weighed then milled with isopropanol in a planetary ball-mill for 5 min. Dried powders were sieved, pressed and heated at 1573 K in air for 48 h. A final step of grinding, sieving and pressing was undertaken before sintering at 1673 K in air for 8 h, achieving sample densities of >95 %th. For characterisation and ion irradiation, samples were ground with silicon carbide grinding papers and polished to a 0.25 μm finish with diamond suspension (MatPrep).

2.2. Ion irradiations

Irradiations with 1 MeV Kr^+ ions, to a fluence of 1×10^{15} ions cm^{-2}, were undertaken at the Surrey Ion Beam Centre (University of Surrey, Guildford, UK), and irradiations with 5 MeV Au^+ ions, to a fluence of 5×10^{14} ions cm^{-2}, were undertaken at the Australian National University (Canberra, Australia). In both cases, irradiations were conducted at room temperature with the ion beam angle of incidence normal to the sample surface. Estimations of the ion irradiation induced damage and electronic-nuclear stopping powers were calculated using SRIM [28], with the 'Detailed Calculation with Full Damage Cascades' option (SRIM 2008) operated with 99,999 ions run for all calculations. Due to the wide range of displacement energies reported for O, Ca, La and Ti, displacement energies were set to 50 eV for all elements to give an estimation of the damage induced [29]. While this is not ideal, no experimental values are available and as with other groups we have used this flat value as a best compromise. We concede dpa values could change if accurate displacement energies could be determined and implemented, as is described by Thomas et al. [30] for the $SrTiO_3$ system. The densities inputted into the SRIM calculations were determined for pristine samples using the Archimedes method. SRIM damage depth profiles for the $x = 0$ and $x = 0.9$ samples irradiated with the 1 MeV Kr^+ and 5 MeV Au^+ conditions are presented in Fig. 2a and b, respectively. For the 1 MeV Kr^+ ion irradiations, the peak damage, estimated using results from SRIM calculations, was 1.38 ± 0.04 displacements per atom (dpa) across the full $Ca_{1-x}La_{2x/3}TiO_3$ compositional range, with the peak damage depth between 300 and 310 nm across the system, and the full damage region extending from the surface to $\approx$ 600 nm. Nuclear stopping was determined to be dominant for Kr^+ ion irradiations, with the electronic-nuclear stopping ratio remaining between 0.76 and 0.8 across the system. For the 5 MeV Au^+ ion irradiations, estimated peak damage was 1.43 ± 0.05 dpa across the entire compositional range. Peak damage depths were found to be between 600 and 640 nm, with the full damage region extending from the surface to $\approx$ 1000 nm. In 5 MeV Au^+ ion irradiations, electronic stopping was determined to be more prevalent, with the electronic-nuclear stopping ratio remaining between 1.18 and 1.22 across the system.

2.3. X-ray diffraction

X-ray diffraction (XRD) was undertaken on the pristine $Ca_{1-x}La_{2x/3}TiO_3$ samples using a Malvern Panalytical X'Pert^3 diffractometer with Cu K_α radiation ($\lambda = 1.5418$ Å) in reflection. Data were

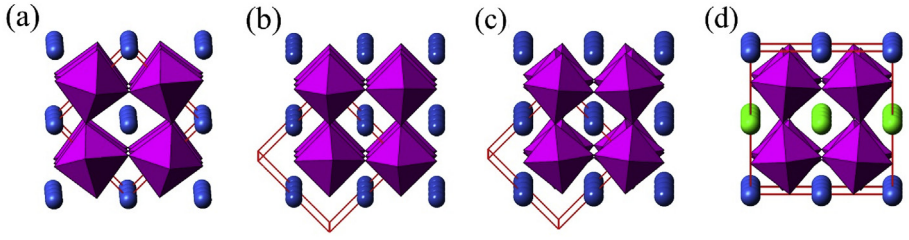

Fig. 1. Structures of the $Ca_{1-x}La_{2x/3}TiO_3$ system with unit cells outlined, as reported by Zhang et al. [21]. A-site Ca/La are represented in blue, with TiO_6 octahedra shown in purple. Green atoms are used to donate A-site vacancy ordering. (a) $x = 0$ Pbnm (b) $x = 0.6$ *Ibmm* (c) $x = 0.7$ *I4/mcm* (d) $x = 0.9$ Cmmm

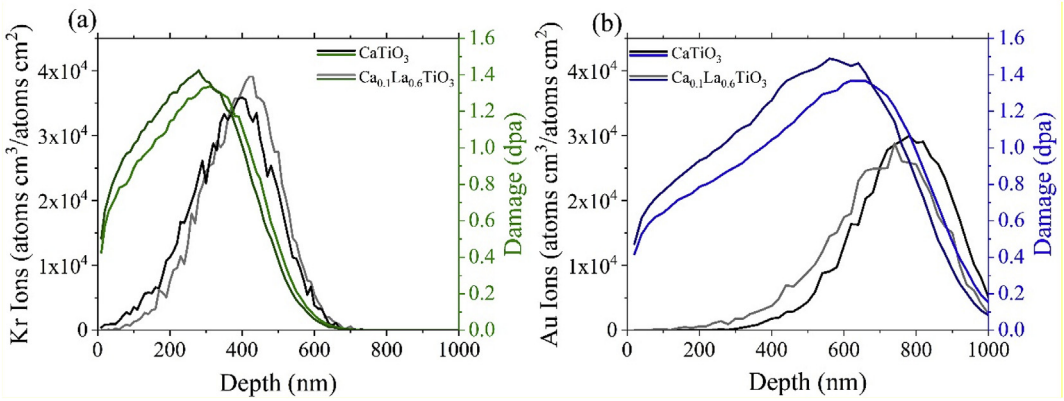

Fig. 2. Estimated displacement damage-depth profiles calculated using SRIM for $Ca_{1-x}La_{2x/3}TiO_3$ samples x = 0 and x = 0.9 irradiated with (a) 1 MeV Kr^+ to a fluence of 1×10^{15} ions cm^{-2} and (b) 5 MeV Au^+ to a fluence of 5×10^{14} ions cm^{-2}.

collected between 10° and 100° with a step size of 0.02° and a step time of 1 s, with X-rays generated at 45 kV, 40 mA. Data were calibrated using an external NIST 640e line position standard. Phase indexing was undertaken by observing the appearance and loss of reflections indicative of in-phase, anti-phase and mixed-phase octahedral tilting [23,31]. Indexing was made with regard to the aristotype perovskites structure, donated by a subscript *p* in $(hlk)_p$ miller indices notation.

2.4. Scanning electron microscopy

Grain size analysis and compositional homogeneity were determined using a Hitachi TM3030 operating with a 15 kV acceleration voltage. Pellets were mounted on aluminium stubs with 12 mm adhesive carbon tabs (Agar). EDS mapping was undertaken using a 10 kV acceleration voltage and a Quantax70 spectrometer with a 154 eV resolution silicon drift detector. Imaging and element mapping were undertaken at 2500× magnification. Grain size analysis was conducted by measuring the area of >100 grains using the ImageJ [32] draw and measure functions to produce a distribution, and an average reported.

2.5. Transmission electron microscopy

Cross-sectional TEM (XTEM) was used to characterise ion irradiation induced damage of selected $Ca_{1-x}La_{2x/3}TiO_3$. Samples were prepared by conventional grinding and polishing using SiC and diamond suspension, followed by final thinning to electron transparency using Ar^+ milling with a Gatan PIPS II. The final thinning energy of the beam was 0.5 keV at 4° from the sample surface. XTEM imaging and electron diffraction pattern analysis was performed using either a FEI Tecnai T20 or JEOL 2010 TEM, both operating at 200 keV. Images and diffraction patterns were captured using a CCD camera. Electron diffraction patterns were taken from both implanted regions and regions that were unaltered by ion irradiation, allowing direct comparison between damaged and undamaged areas within the same sample.

2.6. Glancing-angle X-ray diffraction

Glancing-angle XRD (GAXRD) was carried out using a Malvern Panalytical X'Pert^3 in a parallel beam geometry configuration with Cu K_α radiation ($\lambda = 1.5418$ Å). Data were collected between 20° and 60° with a step size of 0.04° and a time step of 16 s, with X-rays generated with 45 kV, 40 mA. To give a representation of the system as a whole, including varying La contents and phase transitions, Kr^+ and Au^+ ion irradiated samples of compositions x = 0, 0.2, 0.4, 0.5, 0.6, 0.7 and 0.9 were examined using GAXRD. The 5 MeV Au^+ irradiated x = 0.4 sample was omitted due to an experimental error during irradiation that led to an unknown final irradiation fluence. Ion irradiated pellets were placed within a circular cavity machined into a silicon zero background holder to ensure the response detected was only from the ion implanted sample surface. Changes in sample density and X-ray attenuation lengths were induced by La doping and ion irradiation induced amorphisation, leading to variations in X-ray penetration depths in the samples studied. To account for this, patterns were obtained using three incident X-ray angles, Ω, of 0.5°, 1.0° and 1.5° to probe a range of depths. X-ray penetration depths, τ, were calculated using linear attenuation theory, given by equation (1),

$$\Omega = sin^{-1}\left(\tau/3\mu\right), \quad (1)$$

where μ is the linear attenuation coefficient, provided Ω is not below the critical angle, Ω_c, of the incident sample, given by equation (2),

$$\Omega_c = \left(1.6 \times 10^{-3}\right)\rho^{1/2}\lambda \quad (2)$$

For all samples characterised, the condition $\Omega > \Omega_c$ always applied when $\Omega \geq 0.5°$. The linear attenuation coefficient is defined as the length of material travelled through for the X-ray intensity to drop $1/e$ of the initial (≈67%). The factor of 3μ provides ≈99% attenuation, giving the total range over which X-rays penetrate. Calculated X-ray penetration depths for the examined samples are presented in Table 1.

Amorphous fractions were calculated using the Ω = 0.5° patterns by fitting pseudo-Voigt peaks to the amorphous diffuse

Table 1
X-ray penetration depths for $Ca_{1-x}La_{2x/3}TiO_3$ samples as calculated using equation (1) for the three incident angles. Errors represent small variations in density across pellets.

x	X-ray Penetration Depth, τ (±10 nm)		
	Ω = 0.5°	1.0°	1.5°
0	450	900	1350
0.2	420	840	1260
0.4	360	720	1080
0.5	310	620	930
0.6	300	600	900
0.7	280	560	840
0.9	250	500	750

scattering component and $(101)_p$ crystalline reflection, and taking a ratio of the amorphous area to the total fitted area, an example of which is presented in Fig. 3. A single peak fit was used for the $(101)_p$ reflection as it was not possible to differentiate between the K_α contributions to the patterns. This method has been previously used to quantify XRD data by various groups [33–35]. These calculations give a semi-quantitative representation of the induced damage. It should be noted that as X-ray penetration depths are not constant and GAXRD analysis considers a volume of material rather than a specific depth, these values did not give a precise representation of the irradiated region as a whole. For this reason, we termed this analysis as semi-quantitative and this point is further expanded on in section 3.2. Errors quoted are the standard calculated errors from the area fitting process. Lattice parameters of the damaged samples were calculated using a Le Bail refinement and the Bruker TOPAS software, with errors quoted as calculated.

3. Results and discussion

3.1. Pristine characterisation

After synthesis, grain size quantification was undertaken using SEM and compositional homogeneity checked with EDS. Micrographs of the x = 0, 0.2, 0.4, 0.5, 0.6, 0.7 and 0.9 samples, those from which ion irradiation studies were undertaken, are presented in Supplementary Fig. 1. The grain sizes observed varied within each sample, with x = 0 comprising grains of 5–30 μm, the x = 0.2 and 0.4 samples from 10 to 30 μm, and for $x \geq 0.5$ grains were <50 μm. While grain sizes varied, this did show an increase in maximum grain size with La content, likely due to increased diffusion induced by increased A-site vacancy content. EDS maps showed the samples to be homogeneous, with only Ca, La, Ti and O present across each grain and no evidence of secondary phases or unreacted reagents.

Pristine XRD patterns of the $Ca_{1-x}La_{2x/3}TiO_3$ system are presented in Supplementary Fig. 2, with all reflections indexed with regard to the aristotype perovskite structure. Our analysis is in agreement with that by Zhang et al. [23], with the phase transitions reported as *Pbnm* ($a^-a^-c^+$) for $0 \leq x \leq 0.5$, *Ibmm* ($a^-a^-c^0$) for x = 0.6, *I4/mcm* ($a^0a^0c^-$) for $0.7 \leq x \leq 0.8$ and *Cmmm* ($a^0b^0c^-$) for x = 0.9. Further discussion of these observations are available in the supplementary information.

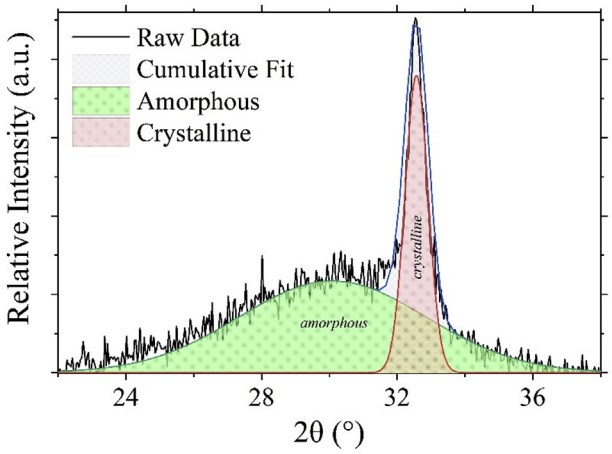

Fig. 3. Example of the pseudo-Voigt peak fitting employed to produce amorphous fractions. The crystalline contribution is donated as *crystalline* in red and the amorphous contribution as *amorphous* in green. The pattern presented is for the x = 0.5 sample irradiated with the 5 MeV Au^+ condition. (For interpretation of the references to colour in this figure legend, the reader is referred to the Web version of this article.)

Zone axis [111] electron diffraction patterns for the x = 0, 0.2, 0.5 and 0.6 samples are presented in Fig. 4a, b, 4c and 4d, respectively. Zone axis [110] and [111] electron diffraction patterns for the x = 0.7 and 0.9 samples are presented in Fig. 4e, f, 4g and 4h, respectively. Aristotype perovskite reflections are indexed with miller indices notation, with reflections originating from in-phase tilting and anti-phase tilting identified with a pink square or green circle, respectively, following the rules reported by Woodward and Reaney [31]. Following their observations, ½(*eoo*) reflections indicate in-phase tilting and ½(*ooo*) reflections indicate anti-phase tilting, using miller indices notation (*e* = even, *o* = odd). The x = 0, 0.2 and 0.5 samples were all found to exhibit ½(*eoo*) tilt reflections in [111] zone axis patterns, confirming the presence of in-phase tilting and the *Pbnm* ($a^-a^-c^+$) structure. The transition from *Pbnm* ($a^-a^-c^+$) to *Ibmm* ($a^-a^-c^0$) was observed through the loss of such in-phase ½(*eoo*) tilt reflections in Fig. 4d for the x = 0.6 [111] pattern.

Reflections indicative of cation/vacancy ordering were identified in the x = 0.7 and 0.9 [110] zone axis electron diffraction patterns presented in Fig. 4e and f, respectively. Anti-phase tilting reflections were observed for both samples, indicated by the ½(*ooo*) reflections denoted by green circles. Additional ½(*oee*) were observed in the [110] patterns for each sample, as indicated by right-pointing purple arrows, and ½(*ooe*) reflections were observed in the same pattern for the x = 0.9 sample, as denoted by left-pointing red arrows. No evidence of in-phase tilting was observed for these samples in [111] zone axis patterns (Fig. 4g and h), so these reflections could not be attributed to mixed-phase tilting. Such additional ½(*oee*) reflections were previously allocated to cation/vacancy ordering in the $Sr_{1-x}La_{2x/3}TiO_3$ x = 0.7 and 0.9 samples [36], and considering previous observations of cation/vacancy ordering in $Ca_{1-x}La_{2x/3}TiO_3$ x = 0.7 and 0.9 samples [23,25], the ½(*oee*) reflections were similarly attributed to ordering or antiparallel cation displacement. The presence of ½(*ooe*) reflections in x = 0.9 samples were similarly credited, with the presence of a layered structure of ordered A-site vacancies observed by Lu et al. [36] to provide double diffraction routes for such reflections.

3.2. Post-ion irradiation characterisation

Bright-field TEM (BFTEM) micrographs of the x = 0, 0.2 and 0.9 samples irradiated with 1 MeV Kr^+ ions are presented in Fig. 5a, c and 5e, respectively. Calculated SRIM profiles for each sample are superimposed, with selective area electron diffraction patterns denoted by white circles for location and an i or ii identifier. The sample surface is indicated by the black/white dashed line and labelled as such. Corresponding GAXRD patterns are presented in Fig. 5b, d and 5f for the x = 0, 0.2 and 0.9 samples, respectively. For the x = 0 sample, lighter regions were observed near the peak of the SRIM profile and were attributed to amorphous or highly damaged material. Dark regions of contrast between the surface and 450 nm from the surface were attributed to regions of crystallinity and confirmed by the electron diffraction pattern taken at point i in Fig. 5a, comprising crystalline reflections and a diffuse ring indicative of damaged material. Fig. 6 shows a magnified XTEM image of these "crystallites", with Moiré fringes observed where crystallites of similar interatomic spacing overlap, confirming the crystalline nature of these regions. Regions of dark contrast between 450 nm and 600 nm were attributed to interstitial-type defect clusters. The maximum damage and range predicted by SRIM was in agreement with the observed results, i.e. range of 600 nm and peak of 310 nm, as confirmed by electron diffraction patterns taken from points i and ii in Fig. 5a. Very faint ½(*ooo*) reflections were identified in the [110] ZAEDP taken at point i in Fig. 5a, suggesting no cubic transition was observed at this fluence. Such a transition has been previously observed, suggesting that an

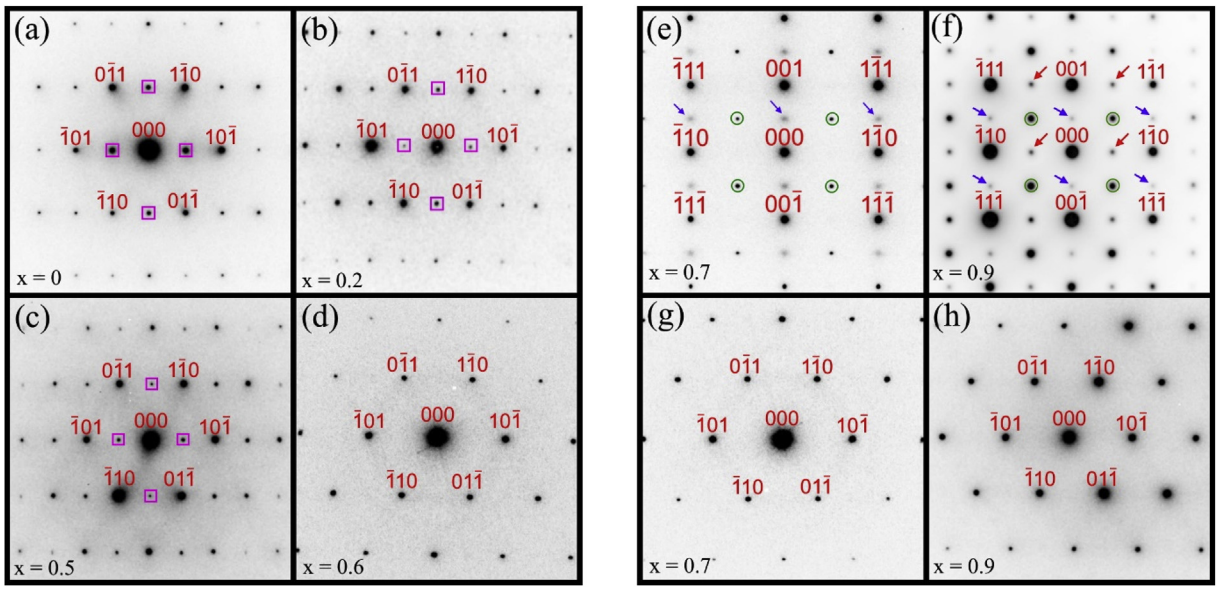

Fig. 4. [111] zone axis electron diffraction patterns for $Ca_{1-x}La_{2x/3}TiO_3$ samples (a) x = 0, (b) x = 0.2, (c) x = 0.5 and (d) x = 0.6. [110] zone axis patterns for $Ca_{1-x}La_{2x/3}TiO_3$ samples (e) x = 0.7 and (f) x = 0.9 and [111] patterns for (g) x = 0.7 and (h) x = 0.9. Aristotype perovskite reflections are labelled, with additional ½(*eoo*) reflections indicated with pink squares. Aristotype perovskite reflections are labelled, with additional ½(*eoo*) reflections indicated with pink squares and ½(*ooo*) indicated with green circles. In (e) and (f), ½(*eoo*) reflections are identified with right-pointing purple arrows and ½(*eeo*) with left-pointing red arrows. (For interpretation of the references to colour in this figure legend, the reader is referred to the Web version of this article.)

increased fluence was required to induce this transition [12,16,19]. The partially damaged nature of the x = 0 sample at 1.34 dpa was in agreement with amorphisation values reported by Meldrum et al. [11] (1.8 dpa) and Smith et al. [16] (2.2 dpa) calculated using *in-situ* methods, however disagreement was found with the bulk 2 MeV Kr^+ ion irradiation study reported by Davoisne et al. [12] (4 dpa). This is discussed further in the next paragraph.

No crystallite formation was observed for the x = 0.2 sample (Fig. 5c). The electron diffraction pattern taken from the peak damage depth by SRIM at point i in Fig. 5b showed no evidence of induced damage, with only crystalline reflections present. This was the case across the SRIM profile. As with the x = 0 sample, the *Pbnm* structure was maintained, as evidenced by the ½(*ooe*) reflections in the [001] ZAEDP taken at point i. These findings were in agreement with the GAXRD patterns observed for the x = 0.2 sample ion irradiated with the 1 MeV Kr^+ condition, representing an increase in resistance to amorphisation when compared to the x = 0 sample. This may also have provided an explanation for the discrepancy with Davoisne et al. [12] whose sample was of the form $(Ca_{0.9}Nd_{0.1})(Ti_{0.9}Al_{0.1})TiO_3$. B-site doping with Al was employed to compensate for A-site Nd doping, however it is likely that a level of A-site deficiency was unintentionally induced, and it is possible that A-site deficiency is responsible for the increased amorphisation fluence within this study.

A BFTEM micrograph of the x = 0.9 sample is presented in Fig. 5e. In this instance, the light contrast from the sample surface to a depth ≈450 nm was indicative of amorphisation, confirmed by the diffuse electron diffraction pattern taken from point i in Fig. 5e. The amorphisation fluence for the x = 0.9 sample was estimated as 0.61 ± 0.2 dpa using the SRIM pattern superimposed on the BFTEM micrograph. At 450 nm, regions of mottled contrast were observed and attributed to interstitial-type end of track defects.

In each instance, the corresponding GAXRD patterns agreed with the BFTEM micrographs. In all cases, as Ω increases the pristine response was greater as X-rays penetrated further past the irradiated surface. This is evidenced by the magnifications presented of the $(101)_p$ peaks, with the pristine and additional 'damaged' reflections indicated. Considering the Ω = 0.5° pattern taken from the 1 MeV Kr^+ irradiated x = 0 sample (Fig. 5b), reflections were observed in the pristine $CaTiO_3$ positions, with additional reflections shifted to higher d-spacings. These reflections were attributed to volume expansion of the unit-cell lattice. Small amounts of diffuse scattering were also observed, in agreement with the diffuse rings observed in the corresponding SAEDP (Fig. 5a at point i). The appearance of both pristine and volume expanded reflections was due to the 450 nm X-ray penetration depth for the x = 0 sample, penetrating past the peak damage depth at 310 nm and probing regions with a reduced dpa. A highly-crystalline response was observed for the x = 0.2 sample at all Ω angles, presented in Fig. 5d. This was in agreement with SAEDP analysis. For Ω = 0.5°, reflections were shifted to a higher d-spacings, with a slight shoulder peak in the $(101)_p$ reflection indexed to a pristine response. At Ω = 0.5° for the x = 0.9 sample (Fig. 5f), the pattern was dominated by diffuse scattering with small amounts of residual crystallinity present. At Ω = 1.0°, a significant crystalline response is observed, corresponding to an X-ray penetration depth of 500 nm. This was surprising, as SAEDP analysis showed the sample was amorphous to a depth of ≈450 nm. Two explanations could explain this behaviour. Either the A-site vacancy content within the sample altered the X-ray penetration depth calculated using linear attenuation theory, or the amorphisation induced by ion irradiation increased the X-ray penetration depth, possibly due to reduced density. By comparison with BFTEM analysis, it appeared the X-ray penetration depth for the irradiated x = 0.9 sample is similar to the x = 0 sample.

GAXRD patterns for the x = 0, 0.2, 0.4, 0.5, 0.6, 0.7 and 0.9 samples irradiated with 1 MeV Kr^+ and 5 MeV Au^+ with an incident X-ray angle of Ω = 0.5° are presented in Fig. 7. Patterns from 1 MeV Kr^+ irradiated samples are presented in green and 5 MeV Au^+ irradiated in blue. The 5 MeV Au^+ irradiated x = 0.4 sample was not presented due to an experimental error during irradiation. A key difference across the two conditions was the increased amorphous fraction for the 5 MeV Au^+ condition when compared to the 1 MeV Kr^+ condition. This may result from the increased electronic

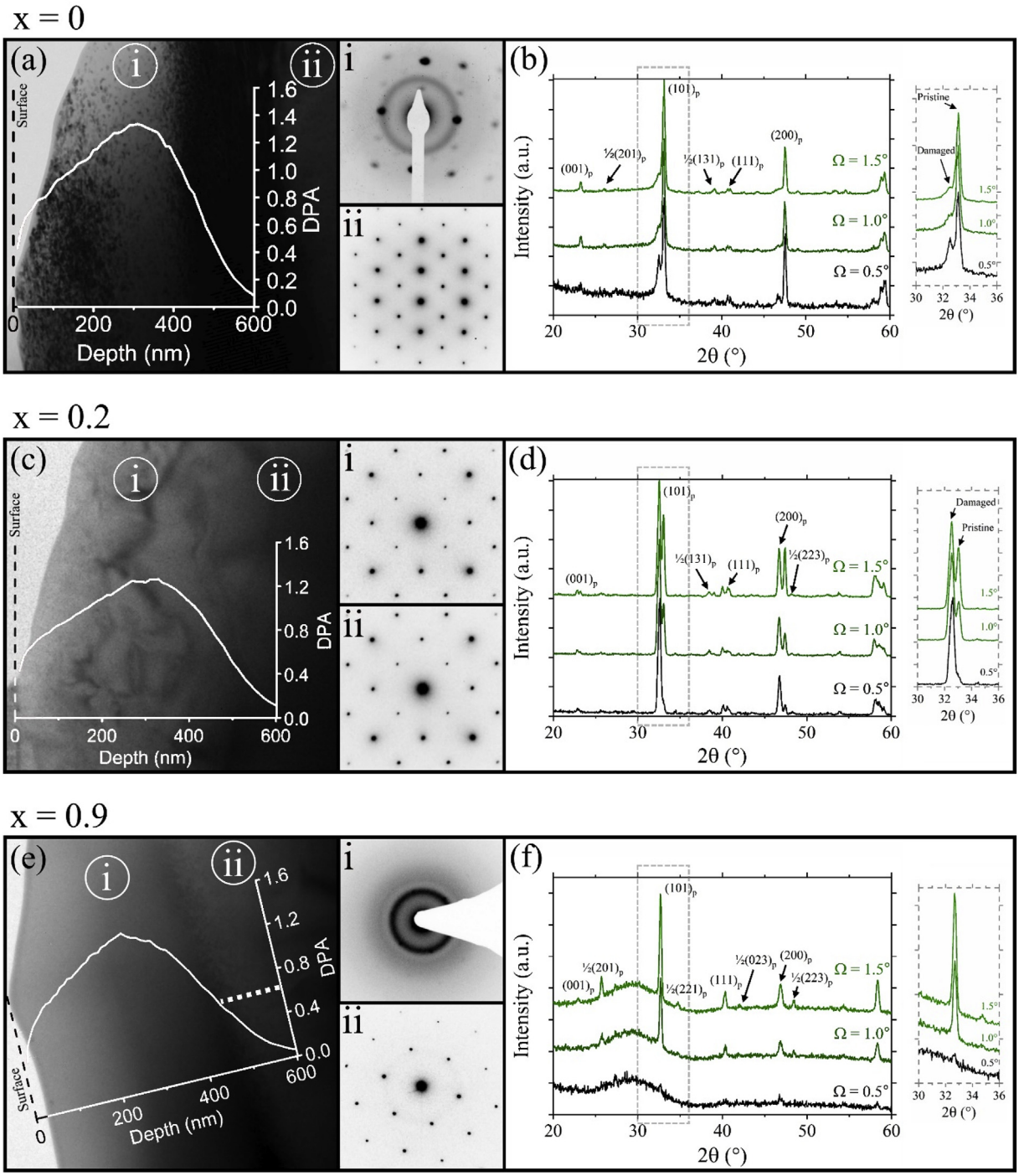

Fig. 5. BFTEM micrographs of 1 MeV Kr^+ ion irradiated $Ca_{1-x}La_{2x/3}TiO_3$ (a) x = 0, (c) x = 0.2 and (e) x = 0.9 samples with associated SAEDPs taken from the regions labelled i or ii, and SAEDPs labelled as such. SRIM profiles for each sample are overlaid on the BFTEM micrographs. Corresponding GAXRD patterns are presented for 1 MeV Kr^+ ion irradiated (b) x = 0, (d) x = 0.2 and (f) x = 0.9 samples for incident X-ray angles of Ω = 0.5°, 1.0° and 1.5°. Plot colours represent changes in incident X-ray angle, with light green for Ω = 0.5°, dark green for 1.0° and black for 1.5°, with each further labelled accordingly. Magnifications of the 30° < 2θ < 36° region are shown for each corresponding GAXRD pattern, as identified by the grey dashed boxes in the full GAXRD patterns. Reflections from pristine material and those corresponding to damaged, volume swollen material are labelled in these magnifications. (For interpretation of the references to colour in this figure legend, the reader is referred to the Web version of this article.)

stopping contribution for the 5 MeV Au^+ condition for all samples, and the previously reported underestimation of damage induction predicted by the SRIM code for ions irradiating compounds with light atoms such as Ti or Ca under electronic stopping conditions [37,38]. Pristine reflections were observed for the 1 MeV Kr^+ samples, with the reasoning for this already discussed. The increased penetration depth of 5 MeV Au^+ ions leads to an extended damage region, and pristine reflections for these samples are not observed at Ω = 0.5°. Considering the previous description of GAXRD patterns taken from the 1 MeV Kr^+ irradiated x = 0, 0.2 and 0.9 samples, Ω = 0.5° patterns were used to give the best representation of the irradiated surface. The diffuse scattering present was used to give an estimation of the level of damage induced in each sample. Amorphous fractions calculated using pseudo-Voigt peak analysis

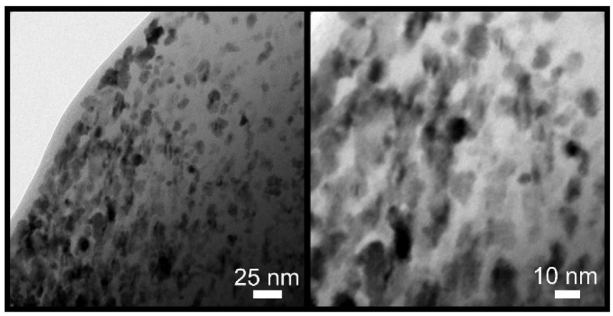

Fig. 6. BFTEM micrographs of the x = 0 sample. Areas of dark mottled contrast show regions of nano-crystalline material amongst highly damaged light contrast regions. Moiré fringes are visible, confirming the crystalline nature of these regions.

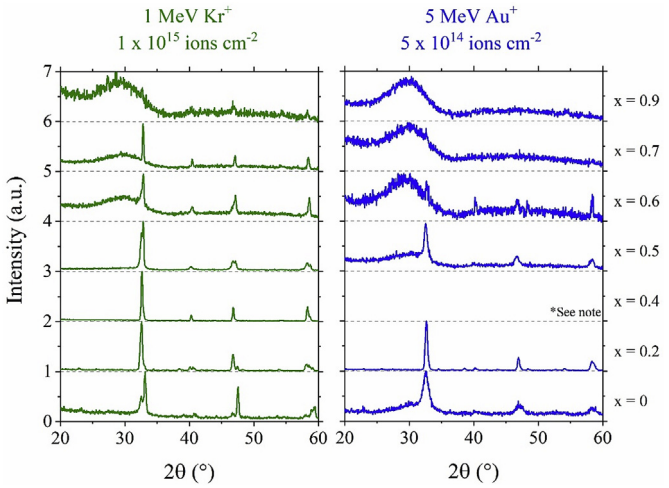

Fig. 7. GAXRD patterns with Ω = 0.5° of 1 MeV Kr^+ and 5 MeV Au^+ ion irradiated $Ca_{1-x}La_{2x/3}TiO_3$ samples as labelled. 1 MeV Kr^+ irradiated samples are presented in green and 5 MeV Au^+ irradiated samples in blue. *Note: the 5 MeV Au^+ irradiated x = 0.4 sample is note presented due to an experimental error during irradiation leading to an undecipherable fluence. (For interpretation of the references to colour in this figure legend, the reader is referred to the Web version of this article.)

are presented in Fig. 8. Under both conditions, the smallest amorphous fraction, and by association the most resistant to amorphisation, can be classified with x as 0.2 = 0.4 > 0 > 0.5 > 0.6 > 0.7 > 0.9. This behaviour lends itself to direct comparison to the

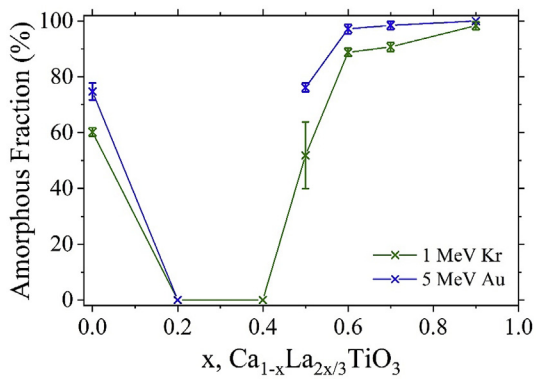

Fig. 8. Semi-quantitative amorphous fractions for the $Ca_{1-x}La_{2x/3}TiO_3$ system irradiated with 1 MeV Kr^+ (green) and 5 MeV Au^+ (blue). (For interpretation of the references to colour in this figure legend, the reader is referred to the Web version of this article.)

work of Smith et al. [21] ($Sr_{1-x}La_{2x/3}TiO_3$) and Whittle et al. [22] ($Ca_{1-x}La_{2x/3}TiO_3$). Within these systems, measurements of the T_c amorphisation showed a reduction in the $0.1 \leq x \leq 0.4$ regions observed to produce a reduced amorphous fraction in this study when, compared with $CaTiO_3$. Furthermore, this agreed with critical fluences reported by Whittle et al. at ≈ 300 K, albeit the x = 0.3 sample could not be amorphised at this temperature. Within these systems, T_c was found to increase at x = 0.5–0.55, and again this was in agreement with a rise in the amorphous fraction calculated for the x = 0.5 sample.

From these findings, it is evident that the mechanisms for increased resistance to amorphisation for $0.1 \leq x \leq 0.4$ and decreased resistance for $0.5 \leq x \leq 0.9$ are present under both irradiation conditions. This is the first observation of such effects in a bulk system, rather than through *in-situ* techniques, and under both nuclear and electronic stopping conditions. Resistance to amorphisation is observed within the highly distorted octahedral networks of the *Pbnm* phase, as opposed to the lesser distorted *Pm-3m* region of the $Sr_{1-x}La_{2x/3}TiO_3$. The x = 0.5 sample, in which such resistance is reduced, also maintains this symmetry, suggesting these effects are unrelated to octahedral tilting or crystal structure. We would agree in this regard that the induction of A-site vacancies is therefore the most likely cause of the increased resistance to amorphisation observed and the reduced barriers to migration for lattice defects. Whittle et al. [22] further argue reduced tolerance for disorder leads to the reduction in amorphisation fluences for $x \geq 0.5$, drawing comparisons with fluorite-type structures that exhibit similar behaviour. The example of Y_2TiO_5 versus $Y_2Ti_2O_7$ is given, in which Y_2TiO_5 more readily recovers from damage due to its increased ability to accommodate disorder through Y locating on both the A and B-sites and readily accommodating anion vacancies. A-site cation/vacancy ordering was observed in the x = 0.7 and 0.9 samples through electron diffraction, and we would agree this likely leads to such marked decreases in the resistance to amorphisation observed, as the structure is less able to tolerate the induction of vacancy defects in a disordered manner. However, a full high-resolution TEM/STEM study of the x = 0.5 and 0.6 structures will likely aid in understanding of this behaviour when considering the system as a whole.

We would offer another possible explanation of this behaviour based on the simulations of Trachenko et al. [14]. Within their work on the amorphisation of $CaTiO_3$, they formulated the hypothesis "*a complex material is amorphisable by radiation damage if its chemistry allows it to form a covalent network*", and explain this process through the increased resistance to amorphisation with Zr content in the $Gd_2Zr_xTi_{2-x}O_7$ solid-solution. The increased covalency of the Ti–O bond as compared to Zr–O more readily produces an amorphous covalent network under ion irradiation, limiting recovery processes within the crystalline network. This theory has been further strengthened through the Compton profile measurements of Bhamu et al. [39], which have shown that Sr–O bonding in $SrTiO_3$ is more ionic than Ca–O in $CaTiO_3$, which computes the covalent network theory through the reported amorphisation doses at 20 K of $SrTiO_3$ (0.93 dpa) and $CaTiO_3$ (0.75 dpa) [11]. It is therefore possible that for $0.1 \leq x \leq 0.4$ within our system of interest, increased A-site recovery or another explanation such as a mass dependence/displacement energy increase is responsible. For $x \geq 0.5$, it is possible that the La–O bond leads to a more readily produced covalent network, reducing the resistance to amorphisation within the system. However, without understanding the true nature of the bonding between the constituent elements of the $Ca_{1-x}La_{2x/3}TiO_3$ system as a whole, this theory cannot be truly tested and remains, as such, a hypothesis. Study of zirconate perovskites systems, namely the $A_{1-x}La_{2x/3}ZrO_3$ (A = Ca, Sr, Ba) systems, would offer more clarity in this area, and experiments are currently being

Table 2
Calculated lattice parameters for the x = 0, 0.2 and x = 0.4 samples after 1 MeV Kr^+ and 5 MeV Au^+ implantation, with pristine values presented for comparison.

Dose	Pristine	1 MeV Kr^+	5 MeV Au^+
		1×10^{15} ions cm^{-2}	5×10^{14} ions cm^{-2}
x = 0			
Volume Expansion (%)	–	4.81 (5)	4.78 (7)
a (Å)	3.8043 (2)	3.863 (5)	3.861 (3)
b (Å)	3.8469 (2)	3.892 (6)	3.891 (5)
c (Å)	3.81835 (3)	3.904 (3)	3.903 (4)
x = 0.2			
Volume Expansion (%)	–	2.11 (8)	1.72 (6)
a (Å)	3.8251 (4)	3.846 (5)	3.841 (7)
b (Å)	3.8497 (3)	3.859 (7)	3.856 (9)
c (Å)	3.8326 (5)	3.884 (5)	3.876 (4)
x = 0.4			
Volume Expansion (%)	–	1.90 (3)	–
a (Å)	3.8445 (1)	3.874 (6)	–
b (Å)	3.8573 (2)	3.864 (3)	–
c (Å)	3.8513 (5)	3.879 (5)	–
x = 0.5			
Volume Expansion (%)	–	1.71 (9)	1.85 (5)
a (Å)	3.8526 (6)	3.873 (6)	3.881 (4)
b (Å)	3.8573 (3)	3.863 (5)	3.862 (7)
c (Å)	3.8513 (3)	3.891 (3)	3.890 (3)

undertaken in this regard.

Volume expansion of the unit cell was observed within the x = 0, 0.2, 0.4 and 0.5 samples under both irradiation conditions, but not for the x = 0.6, 0.7 and 0.9 samples. This is either due to the highly damaged nature of these samples preventing observation of volume swelling, or the inability for these samples to undergo detectable volume swelling prior to amorphisation. Table 2 details the lattice parameter and volume expansion calculated using the Ω = 0.5° GAXRD patterns. Only d-spacing shifted reflections were used for this analysis. Volume swelling in the x = 0 sample remained within error across both conditions at 4.8 ± 0.1%, and similarly for the x = 0.5 sample at 1.8 ± 0.1%. Considering the increased diffuse scattering present in the 5 MeV Au^+ irradiated GAXRD patterns, these values provided evidence of a saturation of volume expansion prior to amorphisation of these samples. If this was not the case, volume swelling would be theoretically higher under the 5 MeV Au^+ condition. This finding agreed with Ball et al. [40], who reported a saturation value of 3.8% for $CaTiO_3$ using neutron irradiation. The use of neutron irradiation was the likely source of discrepancy between our value and that reported by Ball et al. [40]. No such saturation was observed for the highly crystalline x = 0.2 sample, with volume expansion values of 2.11 ± 0.08% and 1.72 ± 0.06% for the 1 MeV Kr^+ and 5 MeV Au^+ conditions, respectively. If a saturation point in this sample exists, it would require a higher induced dpa to observe. Ball et al. [40] further noted the anisotropic nature of the lattice expansion observed. The *b* orthorhombic lattice parameter was observed to expand to a lesser extent than the *a* and *c* parameters for the x = 0, 0.2, 0.4 and 0.5 samples across both irradiation conditions within this study. These values are plotted graphically in Fig. 9, with a consistent trend of $c > a > b$ for parameter swelling. For example, the *b* parameter of the x = 0 sample expanded by 1.2 ± 0.1% across both conditions, with the *a* and *c* parameters increasing by 1.5 ± 0.1% and 2.2 ± 0.1%, respectively. Lattice parameter analysis has shown the pseudo-cubicity of the system increases with La content for x ≤ 0.5 [23] and our own analysis shows the *b* parameter increases by 0.0148 ± 0.0005 Å from x = 0 to 0.5, while increases for the *a* and *c* parameter are observed of 0.0683 ± 0.0004 Å and 0.0659 ± 0.0003 Å. This is teamed with a reduction in the in-phase TiO_6 octahedral tilt angle until no in-phase tilting is observed for x ≥ 0.6. Considering the observations of a cubic phase transition

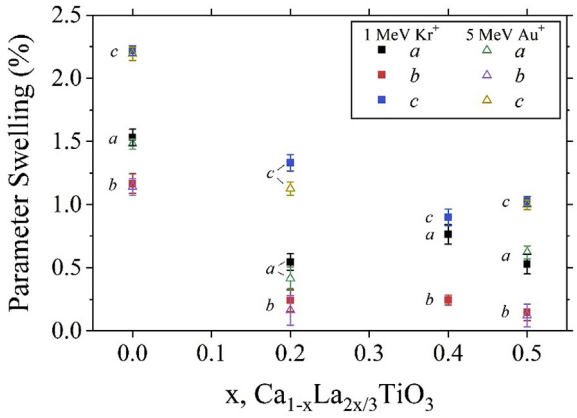

Fig. 9. Percentage change from pristine measurements in *a*, *b* and *c* lattice parameters due to 1 MeV Kr^+ and 5 MeV Au^+ irradiations for the x = 0, 0.2, 0.4 and 0.5 samples.

prior to amorphisation in $CaTiO_3$ [12,16,19], we postulate a similar mechanism drives the *a* and *c* parameters to pseudo-cubicity and reduced in-phase tilting prior to amorphisation, leading to the reduced lattice expansion observed in the *b* parameter.

4. Conclusions

A region of enhanced resistance to radiation damage induced amorphisation has been observed for 0 < x < 0.5 bulk 1 MeV Kr^+ and 5 MeV Au^+ ion irradiated $Ca_{1-x}La_{2x/3}TiO_3$ ceramics, with regard to $CaTiO_3$. A second region of reduced resistance to amorphisation has been observed for x ≥ 0.5. This the first observation of such effects in a bulk system, and is present across both nuclear and electronic stopping regimes. Both mechanisms appear unrelated to structural phase-transitions, with both enhanced and reduced resistance observed within the *Pbnm* structure. This offers confirmation that such effects are likely due to increased A-site cation vacancy mobility onset by intrinsic vacancy induction through La doping, while the potential effects of bonding have been further discussed. Saturation of radiation damage induced lattice expansion was observed for the x = 0 and x = 0.5, reaching maximum expansions of 4.8 ± 0.1% and 1.8 ± 0.1%, respectively. Insufficient damage was induced to confirm a saturation limit in x = 0.2 and 0.4 samples, while no lattice expansion was observed for highly damaged x ≥ 0.6 samples. The orthorhombic *b* lattice parameter was found to saturate at a reduced expansion when compared with the *a* and *c* parameters, possibly due to increasingly pseudo-cubic nature of the samples under irradiation.

Acknowledgements

The authors would like to acknowledge Engineering and Physical Sciences Research Council (EPSRC) for funding under grant numbers EP/L005581/2, EP/K03684X/1 and EP/G037140/1. SML acknowledges funding from the EPSRC funded Nuclear FiRST Doctoral Training Centre. The authors would like to further acknowledge Prof Steve E. Donnelley and Dr Graeme Greaves of the University of Huddersfield for advice and access to microscopy facilities, and Helmholtz-Zentrum Dresden-Rossendorf (Dresden, Germany) and the Australian National University (Canberra, Australia) for access to irradiation facilities.

Appendix A. Supplementary data

Supplementary data to this article can be found online at

https://doi.org/10.1016/j.actamat.2019.09.006.

References

[1] V. Vashook, L. Vasylechko, M. Knapp, H. Ullmann, U. Guth, Lanthanum doped calcium titanates: synthesis, crystal structure, thermal expansion and transport properties, J. Alloy. Comp. 354 (2003) 13–23, https://doi.org/10.1016/S0925-8388(02)01345-2.

[2] V. Vashook, L. Vasylechko, N. Trofimenko, M. Kuznecov, P. Otchik, J. Zosel, U. Guth, A-site deficient perovskite-type compounds in the ternary $CaTiO_3$-$LaCrO_3$-$La_{2/3}TiO_3$ system, J. Alloy. Comp. 419 (2006) 271–280, https://doi.org/10.1016/j.jallcom.2005.09.063.

[3] E. Salje, H. Zhang, Domain boundary engineering, Phase Transitions 82 (2009) 452–469, https://doi.org/10.1080/01411590902936138.

[4] I.-S. Kim, W.-H. Jung, Y. Inaguma, T. Nakamure, M. Itoh, Dielectric properties of A-site deficient peroskite-type lanthanum-calcium-titanium oxide solid solution system, Mater. Res. Bull. 30 (1995) 307–316, https://doi.org/10.1016/0025-5408(94)00142-1.

[5] K. Reeve, J. Woolfrey, Accelerated irradiation testing of Synroc using fast neutrons - first results on barium hollandite, perovskite and synroc B, J. Aust. Ceram. Soc. 16 (1980).

[6] S. Myhra, D.K. Pham, R.S.C. Smart, T.P. S, Dissolution mechanisms of the perovskite and hollandite phases in the SYNROC assemblage, MRS Proc. 176 (1990) 249–254, https://doi.org/10.1557/PROC-176-249.

[7] A.E. Ringwood, V.M. Oversby, S.E. Kesson, W. Sinclair, N. Ware, W. Hibberson, A. Major, Immobilization of high-level nuclear reactor wastes in SYNROC: a current appraisal, Nucl. Chem. Waste Manag. 2 (1981) 287–305, https://doi.org/10.1016/0191-815X(81)90055-3.

[8] A. Jostons, S.E. Kesson, The Synroc strategy for HLW management, Mineral. Mag. 58A (1993) 458–459, https://doi.org/10.1180/minmag.1994.58a.1.238.

[9] H. Mitamura, S. Matsumoto, T. Tsuboi, E.R. Vance, B.D. Begg, K.P. Hart, Alpha-decay damage of Cm-doped perovskite, MRS Proc. 353 (1995) 1405–1412, https://doi.org/10.1557/PROC-353-1405.

[10] T.J. White, H. Mitamura, T. Tsuboi, Rietveld analysis of phase separation in annealed and leach tested Cm-doped perovskite, MRS Proc. 353 (1995) 871–878, https://doi.org/10.1557/PROC-353-871.

[11] A. Meldrum, L.A. Boatner, W.J. Weber, R.C. Ewing, Amorphization and recrystallization of the ABO_3 oxides, J. Nucl. Mater. 300 (2002) 242–254, https://doi.org/10.1016/S0022-3115(01)00733-4.

[12] C. Davoisne, M.C. Stennett, N.C. Hyatt, N. Peng, C. Jeynes, W.E. Lee, Krypton irradiation damage in Nd-doped zirconolite and perovskite, J. Nucl. Mater. 415 (2011) 67–73, https://doi.org/10.1016/j.jnucmat.2011.05.043.

[13] M.J. Hambley, S. Dumbill, E.R. Maddrell, S.C. R, Characterisation of 20 Year old Pu 238 -doped synroc C, MRS Proc. 1107 (2008), https://doi.org/10.1557/PROC-1107-373.

[14] K. Trachenko, M. Pruneda, E. Artacho, M. Dove, Radiation damage effects in the perovskite $CaTiO_3$ and resistance of materials to amorphization, Phys. Rev. B. 70 (2004) 134112, https://doi.org/10.1103/PhysRevB.70.134112.

[15] G.R. Lumpkin, Alpha-decay damage and aqueous durability of actinide host phases in natural systems, J. Nucl. Mater. 289 (2001) 136–166, https://doi.org/10.1016/S0022-3115(00)00693-0.

[16] K.L. Smith, N.J. Zaluzec, G.R. Lumpkin, In situ studies of ion irradiated zirconolite, pyrochlore and perovskite, J. Nucl. Mater. 250 (1997) 36–52, https://doi.org/10.1016/S0022-3115(97)00237-7.

[17] N.C. Hyatt, Plutonium management policy in the United Kingdom: the need for a dual track strategy, Energy Policy 101 (2017) 303–309, https://doi.org/10.1016/j.enpol.2016.08.033.

[18] E.R. Vance, J.V. Hanna, J.H. Hadley, Cation vacancies in perovskites doped with La and Gd, Adv. Appl. Ceram. 111 (2012) 94–98, https://doi.org/10.1179/1743676111Y.0000000037.

[19] W. Sinclair, A.E. Ringwood, Alpha-recoil damage in natural zirconoite and perovskite, Geochem. J. 15 (1981) 229–243.

[20] C. Sabathier, J. Chaumont, S. Rouzière, A. Traverse, Characterisation of Ti and Sr atomic environments in SrTiO3 before and after ion beam irradiation by X-ray absorption spectroscopy, Nucl. Instrum. Methods Phys. Res. B. 234 (2005) 509–519, https://doi.org/10.1016/j.nimb.2005.02.017.

[21] K.L. Smith, G.R. Lumpkin, M.G. Blackford, M. Colella, N.J. Zaluzec, In situ radiation damage studies of La(x)Sr(1-3x/2)TiO(3) perovskites, J. Appl. Phys. 103 (2008), 083531, https://doi.org/10.1063/1.2901183.

[22] K.R. Whittle, M. de los Reyes, R.D. Aughterson, M.G. Blackford, K.L. Smith, P. Baldo, E.P. Ryan, N.J. Zaluzec, G.R. Lumpkin, In-situ irradiation of Ca(1-x)La(2/3x)TiO3 defect perovskites: the role of vacancies in recovery, Materialia 3 (2018) 186–191, https://doi.org/10.1016/j.mtla.2018.08.016.

[23] Z. Zhang, G.R. Lumpkin, C.J. Howard, K.S. Knight, K.R. Whittle, K. Osaka, Structures and phase diagram for the system $CaTiO_3$-$La_{2/3}TiO_3$, J. Solid State Chem. 180 (2007) 1083–1092, https://doi.org/10.1016/j.jssc.2007.01.005.

[24] A.M. Glazer, The classification of tilted octahedra in perovskites, Acta Crystallogr. B 28 (1972) 3384–3392, https://doi.org/10.1107/S0567740872007976.

[25] M. Danaie, D. Kepaptsoglou, Q.M. Ramasse, C. Ophus, K.R. Whittle, S.M. Lawson, S. Pedrazzini, N.P. Young, P.A.J. Bagot, P.D. Edmondson, Characterization of ordering in A-site deficient perovskite $Ca_{1-x}La_{2x/3}TiO_3$ using STEM/EELS, Inorg. Chem. 55 (2016) 9937–9948, https://doi.org/10.1021/acs.inorgchem.6b02087.

[26] C.J. Howard, G.R. Lumpkin, R.I. Smith, Z. Zhang, Crystal structures and phase transition in the system $SrTiO_3$–$La_{2/3}TiO_3$, J. Solid State Chem. 177 (2004) 2726–2732, https://doi.org/10.1016/j.jssc.2004.04.018.

[27] G. King, P.M. Woodward, Cation ordering in perovskites, J. Mater. Chem. 20 (2010) 5785–5796, https://doi.org/10.1039/b926757c.

[28] J.F. Ziegler, M.D. Ziegler, J.P. Biersack, SRIM - the stopping and range of ions in matter, Nucl. Instrum. Methods Phys. Res. Sect. B Beam Interact. Mater. Atoms 268 (2010) 1818–1823, https://doi.org/10.1016/j.nimb.2010.02.091, 2010.

[29] R.C. Ewing, W.J. Weber, J. Lian, Nuclear waste disposal - pyrochlore ($A_2B_2O_7$): nuclear waste form for the immobilization of plutonium and "minor" actinides, J. Appl. Phys. 95 (2004) 5949–5971, https://doi.org/10.1063/1.1707213.

[30] B.S. Thomas, N.a. Marks, B.D. Begg, Defects and threshold displacement energies in $SrTiO_3$ perovskite using atomistic computer simulations, Nucl. Instrum. Methods Phys. Res. Sect. B Beam Interact. Mater. Atoms 254 (2007) 211–218, https://doi.org/10.1016/j.nimb.2006.11.069.

[31] D.I. Woodward, I.M. Reaney, Electron diffraction of tilted perovskites, Acta Crystallogr. Sect. B Struct. Sci. 61 (2005) 387–399, https://doi.org/10.1107/S0108768105015521.

[32] C.A. Schneider, W.S. Rasband, K.W. Eliceiri, NIH Image to ImageJ: 25 years of image analysis, Nat. Methods 9 (2012) 671–675, https://doi.org/10.1038/nmeth.2089.

[33] M. Lang, F. Zhang, W. Li, D. Severin, M. Bender, S. Klaumünzer, C. Trautmann, R.C. Ewing, Swift heavy ion-induced amorphization of $CaZrO_3$ perovskite, Nucl. Instrum. Methods Phys. Res. Sect. B Beam Interact. Mater. Atoms 286 (2012) 271–276, https://doi.org/10.1016/j.nimb.2011.12.028.

[34] D.Y. Yang, C.P. Xu, E.G. Fu, J. Wen, C.G. Liu, K.Q. Zhang, Y.Q. Wang, Y.H. Li, Structure and radiation effect of Er-stuffed pyrochlore $Er_2(Ti_{2-x}Er_x)O_{7-x/2}$ (x=0–0.667), Nucl. Instrum. Methods Phys. Res. B. 357 (2015) 69–74, https://doi.org/10.1016/j.nimb.2015.04.058.

[35] S. Park, M. Lang, C.L. Tracy, J. Zhang, F. Zhang, C. Trautmann, M.D. Rodriguez, P. Kluth, R.C. Ewing, Response of $Gd_2Ti_2O_7$ and $La_2Ti_2O_7$ to swift-heavy ion irradiation and annealing, Acta Mater. 93 (2015) 1–11, https://doi.org/10.1016/j.actamat.2015.04.010.

[36] Z. Lu, H. Zhang, W. Lei, D.C. Sinclair, I.M. Reaney, High-Figure-of-Merit thermoelectric La-doped A-site-deficient SrTiO3 ceramics, Chem. Mater. 28 (2016) 925–935, https://doi.org/10.1021/acs.chemmater.5b04616.

[37] K. Jin, Y. Zhang, Z. Zhu, D.A. Grove, H. Xue, J. Xue, W.J. Weber, Electronic stopping powers for heavy ions in SiC and SiO_2, J. Appl. Phys. 115 (2014), https://doi.org/10.1063/1.4861642.

[38] Y. Zhang, I.T. Bae, K. Sun, C. Wang, M. Ishimaru, Z. Zhu, W. Jiang, W.J. Weber, Damage profile and ion distribution of slow heavy ions in compounds, J. Appl. Phys. 105 (2009), https://doi.org/10.1063/1.3118582.

[39] K.C. Bhamu, A. Dashora, G. Arora, B.L. Ahuja, Nature of bonding in $CaTiO_3$ and $SrTiO_3$: a Compton scattering study, Radiat. Phys. Chem. 81 (2012) 728–734, https://doi.org/10.1016/j.radphyschem.2012.04.010.

[40] C.J. Ball, R.G. Blake, D.J. Cassidy, J.L. Woolfrey, Neutron irradiations effects in perovskite ($CaTiO_3$), J. Nucl. Mater. 151 (1988) 151–161, https://doi.org/10.1016/0022-3115(88)90067-0.